Article

Unveiling Mechanistic Insights and Photocatalytic Advancements in Intramolecular Photo-(3 + 2)-Cycloaddition: A Comparative Assessment of Two Paradigmatic Single-Electron-Transfer Models

Chu Wang, Xiao Liu, Qian Wang, Wei-Hai Fang, and Xuebo Chen*

Cite This: *JACS Au* 2024, 4, 419−431

Read Online

ACCESS | Metrics & More | Article Recommendations | SI Supporting Information

ABSTRACT: The synthesis of 1-aminonorbornane (1-aminoNB), a potential aniline bioisostere, through photochemistry or photoredox catalysis signifies a remarkable breakthrough with implications in organic chemistry, pharmaceutical chemistry, and sustainable chemistry. However, an understanding of the underlying mechanisms involved in these reactions remains limited and ambiguous. Herein, we employ high-precision CASPT2//CASSCF calculations to elucidate the intricate mechanisms regulating the intramolecular photo-(3 + 2)-cycloaddition reactions for the synthesis of 1-aminoNB in the presence or absence of the Ir-complex-based photocatalyst. Our investigations delve into radical cascades, stereoselectivity, particularly single-electron-transfer (SET) events, etc. Furthermore, we innovatively introduce and

compare two SET models integrating Marcus electron-transfer theory and transition-state theory. These models combined with kinetic data contribute to recognizing the critical control factors in diverse photocatalysis, thereby guiding the design and manipulation of photoredox catalysis as well as the improvement and modification of photocatalysts.

KEYWORDS: *1-aminoNB, photo-(3 + 2)-cycloaddition, photoredox catalysis, CASPT2//CASSCF, SET models*
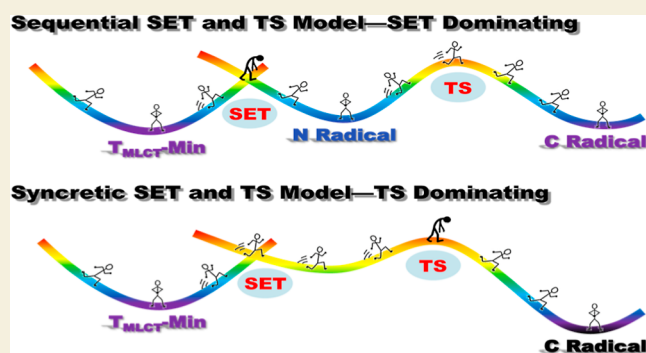
INTRODUCTION

Recent research has highlighted the benefits of incorporating higher fractions of sp^3 carbons (Fsp^3) as surrogates for aromatic rings in drug discovery.[1] Such substitutions have shown significant advantages in terms of their pharmacokinetics and toxicology. Drug molecules with saturated motifs have demonstrated improved potency, solubility, and metabolic stability while exhibiting lower incidences of adverse metabolic processing events such as plasma protein binding and phospholipidosis.[2] This has led to an increased interest in the development of new saturated building blocks, especially caged and bridged polycyclic motifs, offering access to a more diverse chemical space and increased potential for pharmaceutical chemistry.[1c,3,4]

Despite the ease of synthesis, aniline, a commonly used motif in library generation, is prone to deleterious metabolic processing, particularly CYP450 inhibition. Consequently, aniline is recognized as one of the most problematic structural alerts in drug discovery endeavors.[5] An intriguing approach in drug discovery involves the use of general analogues of amine-substituted bridged-ring compounds that share similar sizes and shapes with aniline. These compounds can be visualized as potential aniline bioisosteres,[4a] addressing certain limitations associated with aniline. As a paradigm, the application of 1-aminonorbornanes (1-aminoNBs) has been limited due to the

synthetic challenges posed by S$_N$2 reactions at bridgeheads that result in Walden inversion.[6] On the other hand, alternative approaches that involve multiple steps, including sequential Diels−Alder reactions and Curtius rearrangements, often encounter challenges such as rigorous reaction conditions and relatively low yields.[7] Intramolecular free radical cyclization represents another strategy for synthesizing novel ring systems.[8] Della et al. reported the cyclization of a modified 4-methylenecyclohexylmethyl radical into an intramolecular oxime ether, leading to the formation of bridgehead-substituted aminoNB derivatives.[9] However, the conventional initiation conditions show unfavorable environmental behavior due to the utilization of toxic tin hydride reagents and tend to lead to competitive side reactions. The limited scope of suitable radical precursors also hinders the evolution of this method.
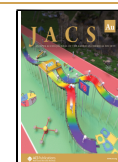
Over the past few decades, the field of organic synthesis has witnessed remarkable advancements through the development of photochemical methodologies, with particular emphasis on visible-light-mediated photoredox catalysis. Notably, researchers represented by MacMillan,[10−17] Yoon,[18−20] Stephenson,[21−24] and some other groups[25−32] have contributed significantly to the establishment of these cutting-edge techniques. This innovative protocol offers a diverse range of methodological strategies for constructing carbon−carbon and carbon−heteroatom bonds or complex chemical building blocks.[10−32] The Stephenson research group made a noteworthy contribution in 2019 by reporting two highly efficient photochemical intramolecular formal (3 + 2)-cycloaddition methods, which delivers the product of 1-aminoNBs under exceptionally mild conditions.[22] The treatment of cyclopropylimines with violet light (390 nm) generates the corresponding Schiff base-protected 1-aminoNBs, i.e., the precursors of C1-NH2 1-aminoNB targets with good yields in the absence of photocatalyst (see Scheme 1A).[22b,33]

Scheme 1. Photochemical (A) and Photocatalytic (B) Intramolecular (3 + 2)-Cycloaddition Reactions of Aminocyclopropanes (AminoCPs) to Synthesize 1-AminoNBs
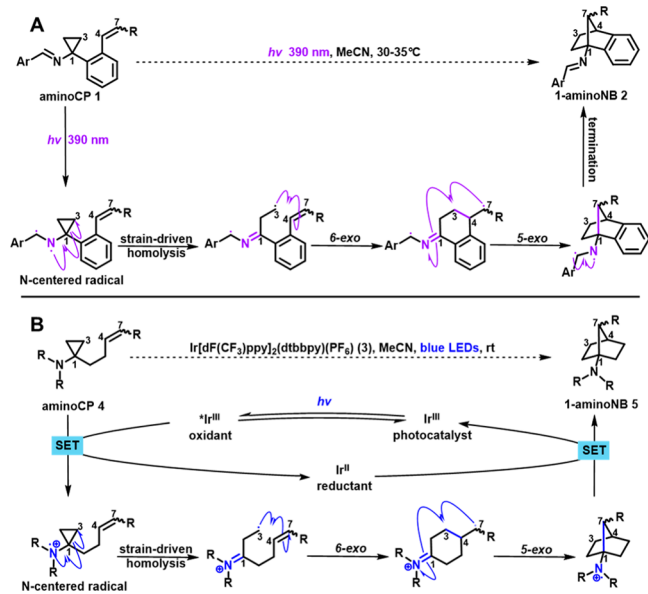
However, relatively high-energy near-ultraviolet light may cause unproductive decomposition reactions, although this approach offers the advantage of not requiring a noble metal catalyst. In a comparative manner, starting materials N,N-dialkylaminocyclopropanes are sensitized by visible-light photocatalyst Ir[dF(CF3)ppy]2(dtbbpy)(PF6) (3) to yield N,N-dialkylaminoNBs (see Scheme 1B).[22c] There is minimal potential for undesirable side reactions arising from the photoexcitation of the substrate itself. The crucial aspect lies in the adaptability between the substrate and the photocatalyst, encompassing factors such as energy levels, redox potentials, and kinetic reaction rates.[10,18,21] In comparison to traditional intramolecular radical cyclization, these methods simplify synthetic procedures, broaden the scope of applicable substrates, and circumvent toxic initiators.[8,9,22] In general, these photochemical or photocatalytic transformations for building 1-aminoNB blocks enrich modern synthetic methodology while holding highly great potential in solving the dilemma of drug metabolism.

Despite the fruitful progress and the proposal of some plausible mechanisms, there remains a dearth of experimental evidence regarding the mechanisms involved in visible-light-mediated photoredox catalysis.[34] Highly active radical intermediates pose challenges for detection even with advanced techniques such as EPR (electron paramagnetic resonance) spectroscopy[35] or time-resolved spectroscopy. This results from the fact that these radicals are often not isolated but engaged in rapid propagation steps, leading to strong interactions with the initiator or catalyst, various substrates, and leaving groups.[36a,b,d] Theoretical investigations can overcome this limitation by offering a means to better comprehend the mechanisms of radical-mediated photochemical reactions. However, an accurate description of electron correlation effects is essential for theoretical investigations to provide valuable insights. Over the past decades, our research group has developed a robust method known as the multiconfiguration perturbation theory together with the orbital localization strategy and the configuration selection strategy and has proven successful in exploring single-electron-transfer (SET)-driven photocatalytic reactions mediated by transition metal or actinide complexes, as well as other photochemical conversions.[36] These research endeavors lay the foundation for the development of theoretical models for photosensitized electron-transfer reactions and contribute to the establishment of an integral strategy for evaluating electron-transfer rates in excited states.

In this study, we build upon our previous work and employ the combined CASSCF (complete active space self-consistent field) and CASPT2 (complete active space second-order perturbation theory) computations associated with the polarizable continuum model (CASPT2//CASSCF/PCM) to investigate the intramolecular photo-(3 + 2)-cycloaddition involved in the synthesis of 1-aminoNBs elaborated earlier. On the one hand, the exemplification of photoredox catalysis reactions serves to refine and enhance the SET theoretical model that we have proposed; on the other hand, it provides new valuable theoretical guidance for photochemical drug design and synthesis and the construction of chemical building blocks.

■ METHODS

The hybrid CASPT2//CASSCF/PCM method was used to calculate the minimum energy profiles (MEPs) for **1**, **1′** and **EC(3−4)**. The computational strategies of orbital localization and configurational selection were applied to the multiconfiguration perturbation calculations in this work, which ensured that the selected orbitals were closely related to the photophysical and photochemical processes based on numerous test calculations and careful examinations. All-electron basis sets were employed for nonmetal atoms, while an ab initio energy-consistent scalar-relativistic pseudopotential with the corresponding basis set, ECP60MWB (8s7p6d2f1g)/[6s5p3d2f1g], was applied for the Ir atom to account for its relativistic effects. Solvent effects were included in all optimizations and intrinsic reaction coordinate (IRC) computations using the polarizable continuum model for the acetonitrile matrix. The phosphorescence lifetimes were evaluated according to the Einstein spontaneous emission formula. The SET rate constants were calculated based on Marcus electron-transfer theory, while the rate constants via an energy barrier in an adiabatic potential energy surface were computed by the transition-state theory. The intersystem crossing (ISC) rates were estimated using the Condon approximation.
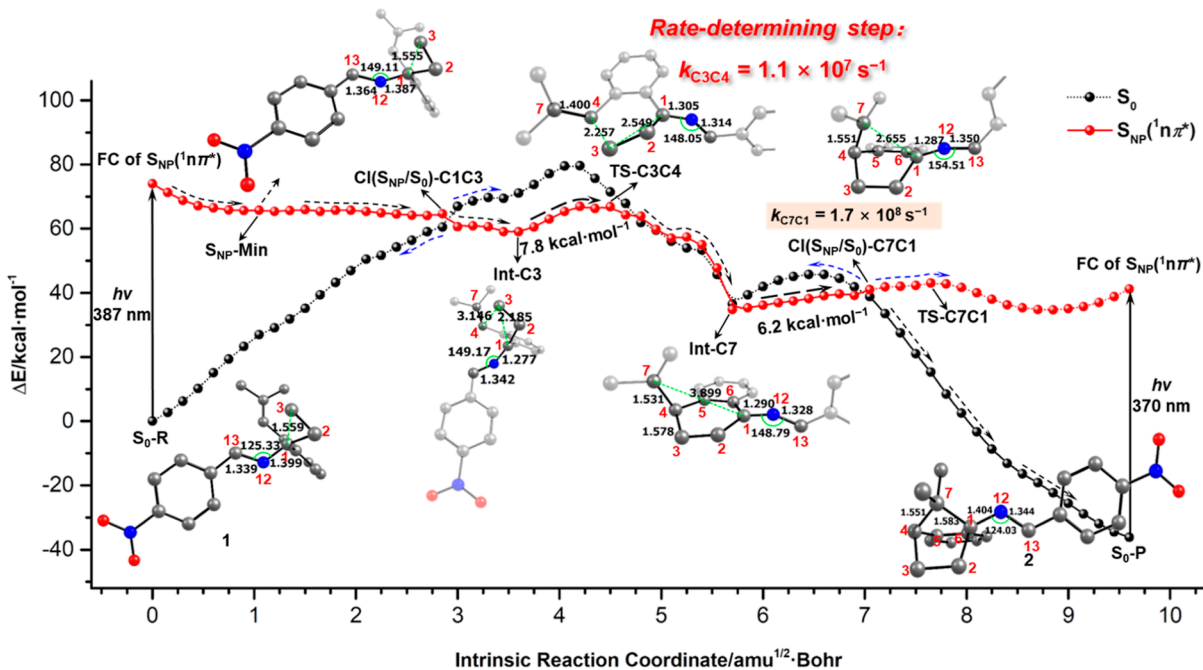
Figure 1. MEPs for the photochemical intramolecular (3 + 2)-cycloaddition reaction of cyclopropylimine **1**. The highlighted characteristic points of **1** are schematically shown together with the numbering scheme in red, the key bond distances (Å), and bond angles (degree). The hydrogen atoms are omitted for clarity. The kinetic data are also provided. These computational results were obtained at the CASPT2//IRC/CASSCF(14e/13o)/PCM level of theory in an acetonitrile solvent.

For more computational details, see Sections S1−S4 in the Supporting Information.

RESULTS AND DISCUSSION

Photochemical Intramolecular (3 + 2)-Cycloaddition Reaction of Cyclopropylimine via a Masked N-Centered Radical Strategy

Our computational analysis begins with the UV−vis absorption properties of benzofused cyclopropylimine **1** (see Section S2.1 in the Supporting Information). The calculated absorption spectrum reproduces the experimentally observed absorption bands and provides a detailed understanding of the electronic transitions involved. The Schiff base system exhibits two prominent absorption bands at 310 nm (oscillator strength f = 0.50) and 252 nm (f = 0.36), along with a much weaker absorption at 387 nm (f = 0.01). These findings align well with the experimental measurements of two intense absorptions centered around 300 and 250 nm, as well as one "invisible" absorption at approximately 385 nm, which becomes apparent upon a substantial increase in concentration, typically by approximately 2 orders of magnitude.[22b] Based on population analyses, the two spectroscopic bright states are assigned as the $\pi \rightarrow \pi^*$ transitions, denoted as $S_{PP1}(^1\pi\pi^*)$ and $S_{PP2}(^1\pi\pi^*)$, respectively, while the dark state is assigned as the n → π^* transition, denoted as $S_{NP}(^1n\pi^*)$. The discrepancy in oscillator strengths can be attributed to an orbital overlap, as the parallel π and π^* orbitals maximize the overlap but the perpendicularity of the n and π^* orbitals necessitates out-of-plane bending. Notably, the species with the singly occupied nitrogen lone pair in the $S_{NP}(^1n\pi^*)$ state bears a resemblance to nitrogen-centered radicals,[37] thus referred to as masked N-centered radicals, which can serve as the electrophilic component capable of reacting with the nucleophile. Moreover, the n → π^* transition of imine **1**, settling in the UVA

region (320−400 nm), displays an evident bathochromic shift relative to carbonyl compounds. For instance, the nπ^* state of chalcone derivatives is usually found in the medium ultraviolet region (280−320 nm).[38] The relatively large resolution between the n → π^* transition and other absorption maxima offers the potential for selective excitation of this specific transition for imine **1**. This effect contributes to excluding other possible unexpected deactivation channels and improves functional group tolerance, distinguishing it from classic carbonyl photochemistry. For example, upon UVB/UVC irradiation, 2′-hydroxy-chalcone undergoes various transitions and multiple photochemical events like excited-state intramolecular proton transfer (ESIPT), which complicates regulation, as evidenced by our previous research.[38]

The relaxation paths for the intramolecular (3 + 2)-cycloaddition reaction of substrate **1** are illustrated in Figures 1 and S7. Upon violet light photoirradiation at 387 nm, **1** is instantaneously promoted in the Frank−Condon (FC) region of the $S_{NP}(^1n\pi^*)$ state. Structurally, the initial decay in this state is characterized by the elongation of the N12=C13 double bond from 1.339 to 1.364 Å and a notable increase in the C1N12C13 bond angle from 125.33 to 149.11°, accompanied by geometric adjustments of chemical bonds within the nitro phenyl ring, which exactly reflects the characteristic of the singly occupied orbitals for the $S_0 \rightarrow S_{NP}(^1n\pi^*)$ transition. These structural changes readily relax the cyclopropylimine to the local minimum of the $S_{NP}(^1n\pi^*)$ state (S_{NP}-**Min**) with an 8.3 kcal·mol^{-1} energy decrease, leading to the generation of a masked N-centered radical intermediate. Because of the inherent strain in the cyclopropane ring, the C1−C3 bond is compelled to undergo a homolytic fragmentation (1.555 → 2.185 Å), resulting in radical migration from the N-center (N12) to the C-center (C3) and the production of the C-center radical intermediate, **Int-C3** (see Figure S6). **Int-C3** shows a growing diradical

characteristic because of enhanced separation of the paired electrons. To our surprise, no energy barrier was found computationally in this process, but a downhill pathway (6.5−7.0 kcal·mol^{-1}) was observed following a flat trajectory. This implies that the entire sequence from the photoexcitation to the complete scission of C1−C3 bond proceeds extremely smoothly with a total of 14.0−16.0 kcal·mol^{-1} energy release, so that can be regarded as a single-step process. Mulliken population analyses reveal that an abundant amount of negative charge initially on N12 becomes dispersed around the π-conjugated moiety after photoexcitation [i.e., S_0-R (−0.4665) → FC of S_{NP} (−0.3943)]. This redistribution of charge enables the singly occupied lone pair on N12 to combine with the nearly coplanar nucleophilic C−C σ bond of the adjacent cyclopropane (C13N12C1C3 dihedral angle: 30.36°) (see Figures S5B and S6). It turns out that throughout the decay from FC of S_{NP} to Int-C3, the N12−C1 bond undergoes concerted shortening (1.399 → 1.277 Å) besides the homolysis of the C1−C3 bond, suggesting the formation of a N12=C1 double bond. Population analyses show that the π bond of the N12=C1 double bond is approximately perpendicular to that of the N12=C13 bond. In other words, the two π bonds are oriented in an upright configuration with respect to each other. In accordance with potential energy scans, geometry optimizations, and CASPT2//CASSCF calculations, it was found that when the initial structures of **1** attempted to incorporate the C−C σ bond of the cyclopropane into the N12=C13 double bond to form a three-center−four-electron (3c−4e) π bond[39] instead of a N12=C1 double bond, the barrier for the homolysis of the C1−C3 bond would be promoted to about 22.0 kcal·mol^{-1} that was exceedingly difficult to surmount (see Figure S5A). The initial conformations of **1** thus play a crucial role on the progress of this photoreaction (see Section S2.2 in the Supporting Information for more details). In general, the synergism of the charge redistribution from S_0 to S_{NP}(^{1}nπ*) and the strain present in the cyclopropane ring facilitates the breaking of the cyclopropyl C−C bond through a barrierless pathway. Note that a competitive nonradiative inactivation channel for S_{NP}(^{1}nπ*) is observed as a rapid internal conversion when the C1−C3 bond is elongated to 1.953−1.984 Å, denoted as CI(S_{NP}/S_0)-C1C3. S_{NP}(^{1}nπ*) energetically degenerates with S_0 in this conical intersection region, and through this channel, the system will return swiftly to the initial reactant, S_0-R, along a steep, downhill pathway of the ground state. Therefore, to ensure that most substrate is transformed into intermediate Int-C3, imine **1** needs to be repeatedly subjected to photoexcitation, which seriously reduces the quantum yield of this photoreaction. As a critical consequence, the masked N-centered radical intermediate is almost unlikely to be entrapped due to its rapid deactivation to either the reactant or the carbon radical intermediate, but Int-C3 exhibits a different behavior and can potentially be detected.

The exposed carbon radical centered on the C3 atom imposes a strong attraction on the intramolecular electron-deficient olefin, acting as a nucleophile. This interaction drives the movement of C3 toward the olefin moiety. The C3-centered n orbital is gradually converted into the σ orbital between C3 and C4. As the distance between C3 and C4 is reduced to about 2.257 Å (TS-C3C4), a conspicuous energy drop will occur in the energy levels of both the S_0 and S_{NP}(^{1}nπ*) states. Simultaneously, the energetic splitting

gradually diminishes between these states. The complete C3−C4 bond formation (3.146 → 1.578 Å) results in the collapse of the π orbital of olefin associated with the breakage of the C4=C7 double bond (1.360 → 1.531 Å) by overcoming a medium barrier (TS-C3C4: 7.8 kcal·mol^{-1}). Meanwhile, a stable six-membered ring skeleton is constructed successfully, accompanied by the radical migration from the imine-centered C3 radical (Int-C3) to the olefin-centered C7 radical (Int-C7) (see Figure S6). This cyclization can be characterized as 6-exo-trig, whose first prefix means six atoms in the forming ring, the second indicates that the breaking bond is exocyclic to the forming ring, and the third signifies the sp^2 hybridization (trigonal) at the ring closure point.[8] Similarly, when the carbon radical centered on the C7 atom is unmasked, an intense attraction between C7 and the intramolecular electron-poor N12=C1 double bond prompts the C7-centered n orbital to integrate into the C7−C1 σ orbital (3.899 → 1.604 Å) by surmounting a middle-sized barrier (TS-C7C1: 8.2 kcal·mol^{-1}). However, another internal conversion region is determined between S_{NP}(^{1}nπ*) and the ground state when the C7−C1 distance decreases to around 2.655 Å, denoted as CI(S_{NP}/S_0)-C7C1, which allows for an effective decay to the ground state. The existence of CI(S_{NP}/S_0)-C7C1 lowers the C7−C1 bonding energy barrier from 8.2 to 6.2 kcal·mol^{-1} and ultimately accomplishes the generation of the end product (S_0-P) along a downhill path on the ground state. This process is characterized by various structural adjustments besides the generation of the C7−C1 bond (3.899 → 1.583 Å), including the breakage of the N12=C1 double bond (1.290 → 1.404 Å), the decreased C1N12C13 bond angle (148.79 → 124.03°), the restoration of the N12=C13 double bond (1.328 → 1.344 Å), as well as the formation of a double-five-membered bridged-ring moiety (5-exo-trig).

According to TST (transition-state theory) calculations, the rates of the 6-exo-trig and 5-exo-trig radical cyclization steps can be estimated as 1.1×10^7 and 1.7×10^8 s^{-1}, respectively, indicating that the 6-exo-trig radical cyclization serves as the rate-determining step for the overall reaction. Notably, product 1-aminoNB (**2**) has analogous absorption properties with reactant **1** (see Section S2.1 in the Supporting Information), suggesting the possibility of the inverse reaction occurring simultaneously, with **2** as the reactant and **1** as the product. However, by backward analyses of the MEPs, we found that a sizable barrier for the breaking of the C3−C4 bond (>30.0 kcal·mol^{-1}) turned off the energy-accessible channel after the formation of Int-C7. As a result, the system returns to S_0-P (**2**) from S_{NP}(^{1}nπ*) to S_0 via CI(S_{NP}/S_0)-C7C1. The estimated rate of inverse reaction (10^{-11} to 10^{-10} s^{-1}) is 17−18 orders of magnitude lower than that of the forward reaction (~10^7 s^{-1}), thereby ensuring the forward equilibrium shift for this photoreaction. Unfortunately, the absorption of product **2** also inevitably reduces the quantum efficiency of this photoreaction. On the whole, this violet-light-mediated intramolecular (3 + 2)-cycloaddition strategy takes over the kinetically unfavorable mechanistic pathway under thermal control (barrier: ~80 kcal·mol^{-1}) to afford 1-aminoNBs efficiently.

Potential Origin of Diastereoselectivity for C7-Alkyl Mono-Substituted Cyclopropylimine in the Intramolecular (3 + 2)-Cycloaddition Reaction

Stephenson et al. discovered an intriguing experimental phenomenon that the 1-aminoNB product was in favor of
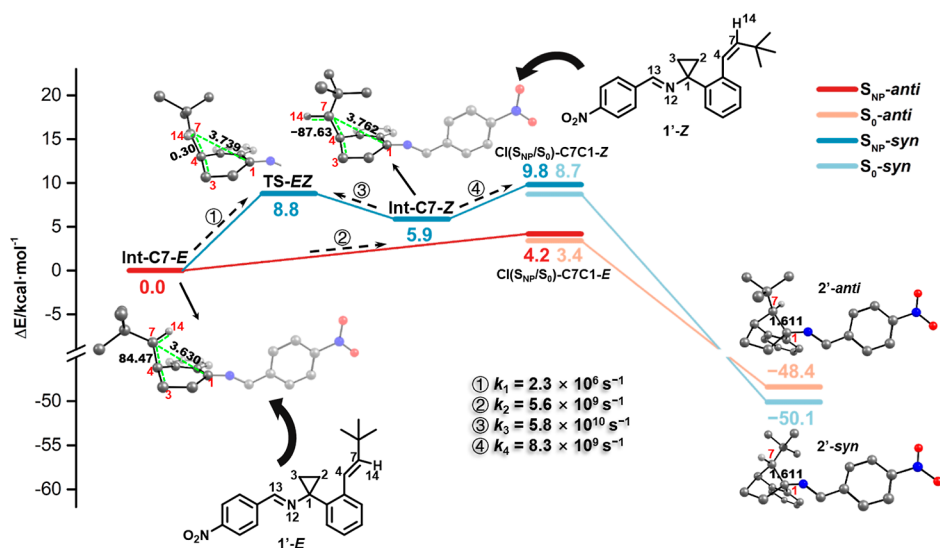
Figure 2. Structural evolutions along the critical points of relaxation paths with their relative energies (kcal·mol^{-1}) for **1′** starting from **Int-C7**. Hydrogen atoms are omitted for clarity, except H14.

the anti-configuration for C7-alkyl monosubstituted cyclopropylimine regardless of whether the original olefin geometry was the *E*-isomer or the *Z*-isomer.[22b] Two cis−trans isomers, **1′**-*E* and **1′**-*Z*, were inspected to explore the origin of this diastereoselectivity by CASPT2//CASSCF calculations (see Figures 2 and S8). Starting from the C7 radical intermediate of **1′**-*E*, i.e., **Int-C7**-*E*, the system can overcome a medium energy barrier (4.2 kcal·mol^{-1}) and subsequently decay to the product **2′**-anti along a downhill relaxation path through **CI(S$_{NP}$/S$_0$)-C7C1**-*E*, in combination with the formation of a C7−C1 bond (3.630 → 1.611 Å). However, the production of **2′**-*syn* requires an additional rotation of the C4−C7 bond (C3C4C7H14 dihedral angle: 84.47 → −87.63°) to generate another C7 radical intermediate, denoted as **Int-C7**-*Z*. The rotation introduces a little high barrier (8.8 kcal·mol^{-1}) owing to the eclipsed conformation of transition state **TS**-*EZ* (C3C4C7H14 dihedral angle: ∼0°). TST calculations reveal that the rotation of the C4−C7 bond is less effective than the shortening of the C1−C7 bond (2.3 × 10^6 s^{-1} for the former, 3−4 orders of magnitude smaller than the latter 5.6 × 10^9 s^{-1}), leading to the predominance of **2′**-*anti* product (3.0:1 *anti*:*syn* dr measured in the experiment).

As for the **1′**-*Z* system, the less stable intermediate, **Int-C7**-*Z*, will get involved immediately after the 6-*exo*-trig radical cyclization step. In this case, C7 can be smoothly bonded to C1 to form the **2′**-*syn* product through **CI(S$_{NP}$/S$_0$)-C7C1**-*Z* by surmounting a barrier of 3.9 kcal·mol^{-1}. Alternatively, the C4−C7 bond can competitively rotate by surpassing a lower barrier of 2.9 kcal·mol^{-1}. The efficiency of bond rotation slightly exceeds that of instant transformation (5.8 × 10^{10} and 8.3 × 10^9 s^{-1}, respectively), which triggers off the conformational change from **Int-C7**-*Z* to the more stable intermediate, **Int-C7**-*E*, that prefers the **2′**-*anti* product. Additionally, the inverse reaction of the **2′**-*syn* product on the S$_{NP}$(^{1}nπ*) state will continuously increase the concentration of **Int-C7**-*Z*, facilitating the equilibrium shift from **Int-C7**-*Z* to **Int-C7**-*E*. It is the mutual transformation of intermediates and the occurrence of inverse reaction for **2′**-*syn* that allow the **1′**-*Z* system to possess a similar tendency with **1′**-*E* toward the **2′**-*anti* product. In summary, diastereoselectivity for C7-alkyl-

monosubstituted cyclopropylimine primarily originates from kinetic control.

Photophysical Properties for Isolated Photocatalyst 3

To elucidate the origin of the ultraviolet−visible-light absorption band of photosensitizer **1**, its absorption spectrum was simulated at the CASPT2//CASSCF/PCM level of theory (see Section S3.1 in the Supporting Information). Qualitatively, the near-degenerate occupied d orbitals (t$_{2g}$) of the Ir(III) metal center have three electron pairs with an equal probability of being promoted to the unoccupied π* orbitals of the three similar ligands upon irradiation, i.e., S$_0$ → S$_{MLCT}$ (d → π*), resulting in a total of nine similar metal-to-ligand charge-transfer (MLCT) excited states. They should have appeared in close proximity to each other at the spectrum. However, as shown in Figure S10, these nine MLCT states locate at different positions in the absorption spectrum, giving rise to a broad absorption band spanning over 200 nm, ranging from 240 to 480 nm. The strong couplings driving the linear combinations of nine MLCT states significantly extend the absorption band to the visible range and simultaneously improve the intensity of the maximum MLCT absorption (368 nm, oscillator strength *f* = 0.18, highlighted with a red line in Figure S10). The maximum absorption with acceptable intensity is principally responsible for the visible absorption band that can be utilized directly in photoredox catalysis. The calculated spectrum is in good agreement with the experimentally observed band ranging from 250 to 500 nm with the maximum absorption centered at 370−380 nm. Careful comparisons reveal that the computed vertical excitation energies of ILCTs (intraligand charge transitions), MLCTs, and LLCTs (ligand-to-ligand charge transfers) together with their oscillator strengths well reproduce the features of experimental spectrum for photocatalyst **3**.[40] Notably, the absorption band predicted by TDDFT calculations exhibits a relatively narrow range compared to the experimental findings, while the CASPT2//CASSCF calculations give a better description[41] because the latter method takes dynamic correlation effects and couplings into account preferably.[42]
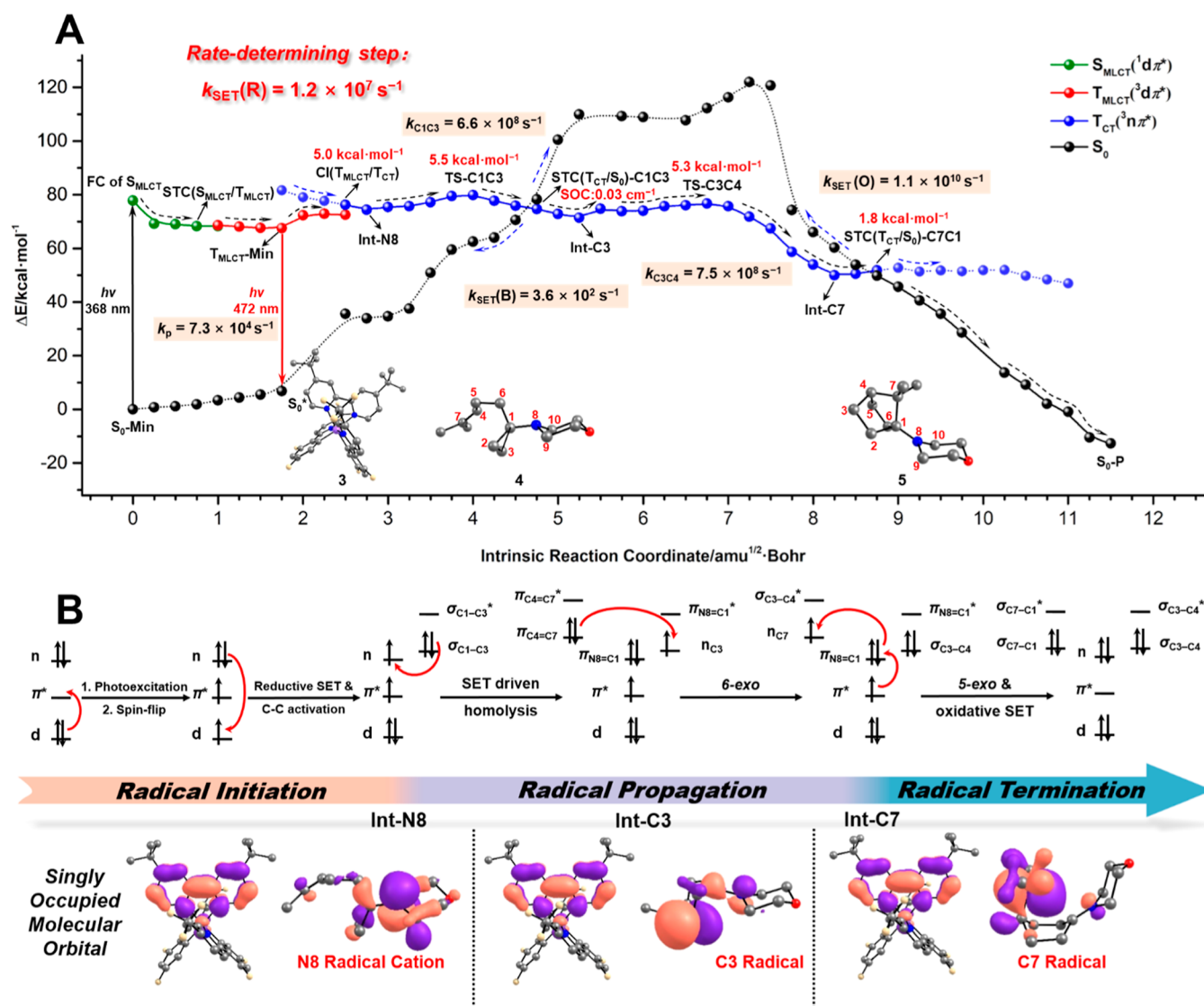
Figure 3. (A) MEPs for the intramolecular (3 + 2)-cycloaddition reaction of cyclopropylamine **4** to produce 1-aminoNB **5** mediated by photocatalyst **3**. The barriers of **CI(T$_{MLCT}$/T$_{CT}$)**, **TS-C1C3**, **TS-C3C4**, and **STC(T$_{CT}$/S$_0$)-C7C1** are defined to compare with the corresponding intermediates **T$_{MLCT}$-Min**, **Int-N8**, **Int-C3**, and **Int-C7**, respectively. The hydrogen atoms and PF$_6^-$ have been omitted for clarity. The kinetic rates are also provided. These computational results were obtained at the CASPT2//IRC/CASSCF(14e/11o)/PCM level of theory in acetonitrile solvent. (B) Electron shifts among the orbitals involved in the photocatalysis and evolution of singly occupied molecular orbitals (SOMOs) of reductive triplet state.

Under visible light irradiation, photocatalyst **3** is initially populated in the FC region of the MLCT singlet state S$_{MLCT}$(^{1}dπ^*) with the maximum absorption (368 nm, f = 0.18) and rapidly decays to its minimum S$_{MLCT}$(^{1}dπ^*)-**Min** that energetically degenerates with the MLCT triplet state T$_{MLCT}$(^{3}dπ^*) at the singlet−triplet crossing **STC(S$_{MLCT}$/T$_{MLCT}$)** (see Figure S11). Due to strong relativistic effects of Ir metal, the spin−orbit coupling constant (SOC) in the STC region is calculated to be about 50.0 cm^{-1}, which allows a fast intersystem crossing (k_{ISC} = 19.0 × 10^{12} s^{-1}) and relaxes the low-lying emissive T$_{MLCT}$(^{3}dπ^*) state to its minimum T$_{MLCT}$(^{3}dπ^*)-**Min**, producing a 472 nm phosphorescence emission. The picosecond-scale intersystem crossing inhibits the fluorescence emission usually at the nanosecond scale and shortens the phosphorescence lifetime to the microsecond level (13.7 μs).[43] Our calculations are in consistent with the experimental results that the phosphorescence emission of **3** is measured at λ_{em} = 470 nm in acetonitrile solution characterized by a long lifetime (2.3 μs),[40] which provides a wide time window for the competitive coexistence of a photocatalysis reaction channel. The calculated lifetime is about 1 order of magnitude longer than the actual value since nonradiative events cannot be neglected in practice (the photoluminescence quantum yield of **3** is around 68%). Moreover, the energy gap between T$_{MLCT}$(^{3}dπ^*)-**Min** and the ground-state minimum S$_0$-**Min**, i.e., the adiabatic excitation energy of **3**, amounts to about 70.0 kcal·mol^{-1} (see Figure S11 and Table S4). However, there are minimal disparities in structural parameters between T$_{MLCT}$(^{3}dπ^*)-**Min** and S$_0$-**Min**, as quantitatively evidenced by a mere 0.05 Å root-mean-square deviation (RMSD) value for their structures (see Figures S12 and S13). This negligible structural variation between the excited state and the ground state facilitates such an effective ground-state recovery of the photocatalyst in the repeated absorption−emission or photocatalytic cycles that optical energy can be fully exploit.
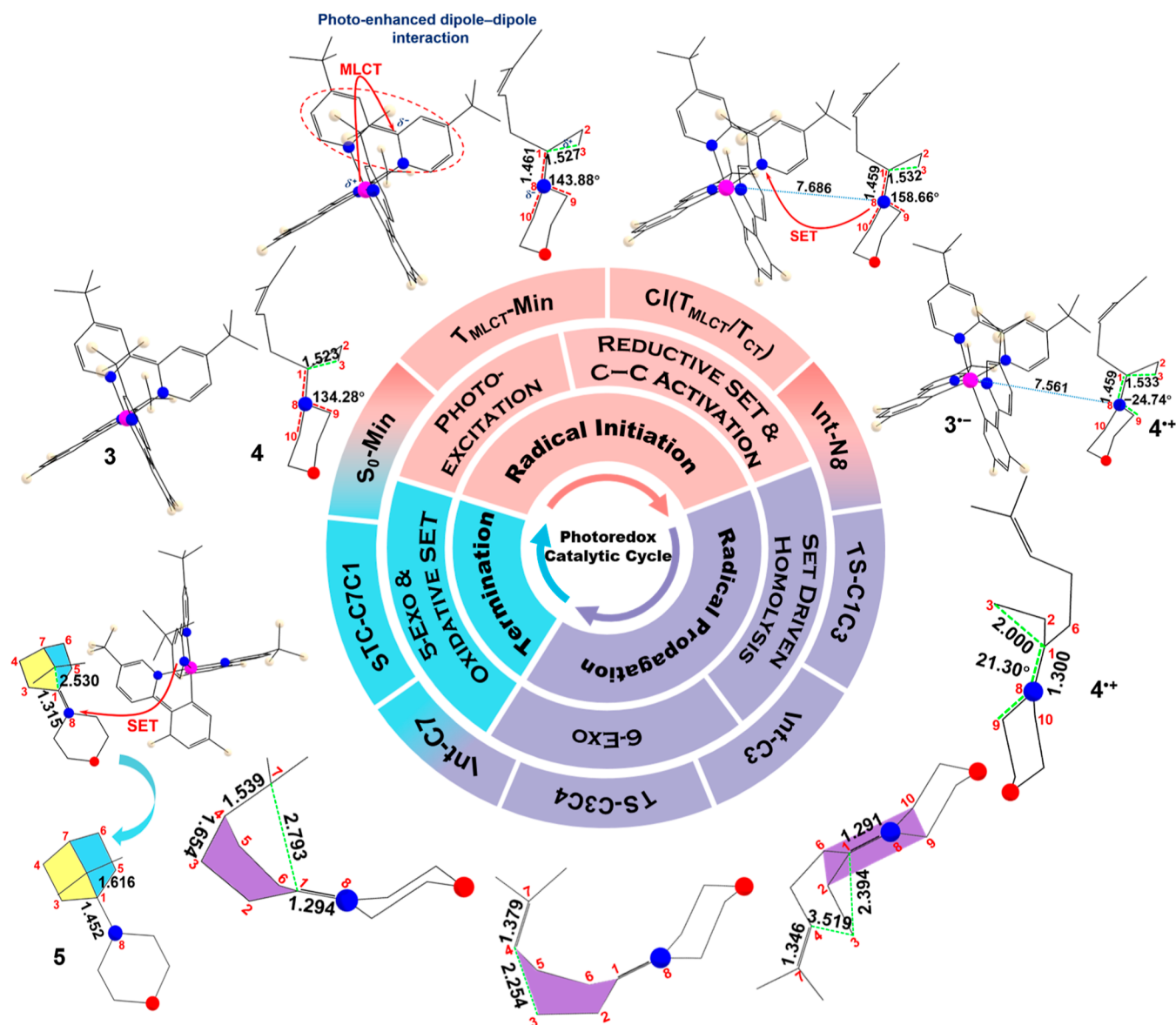
Figure 4. Summary of the photocatalytic cycle for the intramolecular (3 + 2)-cycloaddition reaction of cyclopropylamine **4** mediated by the photocatalyst **3**. The geometries at the highlighted characteristic points are given along the reaction path in Figure 3A with their key bond distances (Å), dihedral angles (degree), and some other structural features. Photocatalyst **3**$^{•-}$ is omitted for **TS-C1C3**, **Int-C3**, **TS-C3C4**, and **Int-C7** (see Figure S17 for their complete geometries). All hydrogen atoms and PF_6^- are omitted for clarity.

Reductive SET-Driven Carbon Radical Formation via the Strain-Driven Homolysis of the Cyclopropane Ring

Unlike the case of the isolated photocatalyst, in the presence of tertiary amine substrate, the intermolecular dipole–dipole interaction between photocatalyst **3** and amine **4** is instantaneously triggered by the photoenhanced dipole moment of the MLCT excitation from the Ir(III) center to the di-*tert*-butyl bipyridine ligand (dtbbpy). The interaction induces an opposite dipole moment, mainly distributed in the $(C1-C2-C3)^{\delta+}-N8^{\delta-}$ structural region of amine **4**, which expands the electron donation ability of N8 (see Table S6). Along the decay from **FC** of S_{MLCT} to T_{MLCT}-**Min** for the **3**–**4** encounter complex, denoted as **EC(3–4)**, the C1–C3 bond is initially activated (1.523 → 1.527 Å) accompanied by a degree of planarization of amine **4** (C9N8C1C10 dihedral angle: 134.28 → 143.88°) owing to the photoenhanced dipole– dipole interaction and the charge redistributes from S_0-**Min** to

T_{MLCT}-**Min** (see Figures 3, 4, and S16). Then, a moderate barrier of 5.0 kcal·mol^{-1} is overcome to drive the further C1– C3 bond elongation (1.527 → 1.532 Å) and the slightly N8– C1 bond shortening (1.461 → 1.459 Å) in combination with the further remarkable planarization of amine **4** (C9N8C1C10 dihedral angle: 143.88 → 158.66°). This preadjusted step promotes the lone pair electrons of N8 to the lowest-lying ligand π^* orbital of T_{MLCT}-**Min** for the Ir catalyst[36b] and brings the catalytic system to the conical intersection region between the T_{MLCT} precursor state and the **EC(3–4)** intermolecular charge-transfer triplet state $T_{CT}(^3n\pi^*)$, denoted as **CI(T_{MLCT}/ T_{CT})**. Since photocatalyst **3** acts as an electron acceptor, this process is named reductive SET hereafter. **CI(T_{MLCT}/T_{CT})** provides an energetically accessible channel to trigger the reductive SET and the radical initiation, thereby generating the zwitterionic complex of **3**$^{•-}$–**4**$^{•+}$ with a diradical configuration. Because of the intermolecular Coulomb interaction, cation **4**$^{•+}$

Scheme 2. Sequential SET and TS Model for the Reduction Reaction of Intramolecular (3 + 2)-Cycloaddition (A) and Syncretic SET and TS Model for the Reduction Reaction of Amide-Directed Distal sp³ C−H Functionalization (B) Summarized Together with Their Key Kinetic Parameters in Polar Acetonitrile[a]
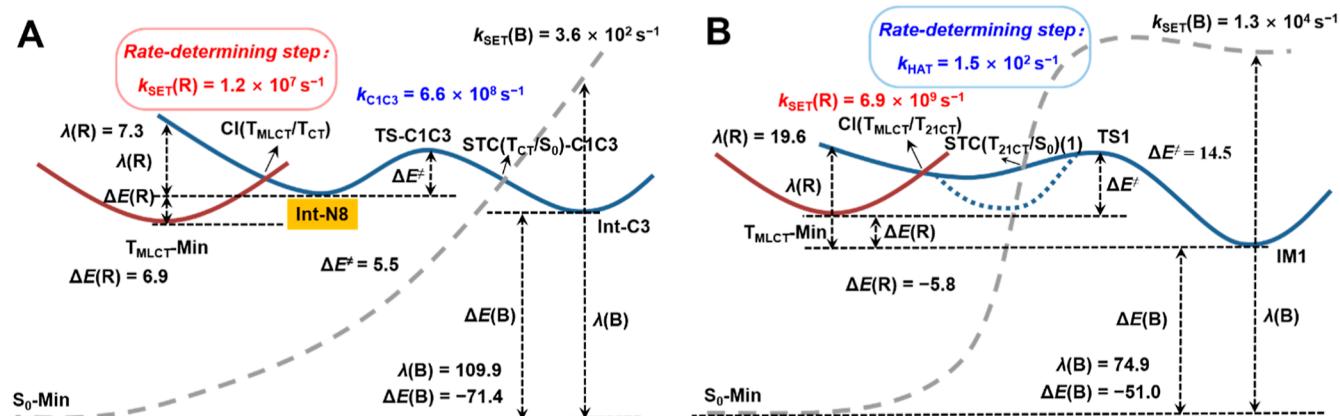
[a]The reorganization energy of reductive SET $\lambda(R)$ and back SET $\lambda(B)$, the potential energy change of reductive SET $\Delta E(R)$ and back SET $\Delta E(B)$ as well as the activation energy $\Delta E^{\ddagger}$ are given in kcal·mol⁻¹.

approaches anion $3^{\bullet-}$ (Ir−N8 distance: 7.686 → 7.561 Å), during which the C1−C3 bond is eventually activated (1.532 → 1.533 Å) with a concomitant planarization (C9N8C1C10 dihedral angle: 158.66 → 160.30°) induced by the N-centered radical cation for $4^{\bullet+}$. These structural reorganizations relax the catalytic system to a local minimum momentarily, producing a relatively stable amine radical cation intermediate, denoted as **Int-N8** (see Figures 3, 4, and S16).[44] Mulliken population analyses indicate that a generous amount of negative charge is transferred from N8 to photocatalyst **3** after the reductive SET [i.e., N8: T_{MLCT}-**Min** (−0.5527) → **Int-N8** (−0.0296) and Ir-dtbbpy: T_{MLCT}-**Min** (0.3553) → **Int-N8** (−0.2693)], which allows the singly occupied lone pair of N8 to be capable of reacting with the nucleophilic C−C σ bond of the adjacent cyclopropane (see Table S6 for more details). Furthermore, **Int-N8** shows an obvious increase in dipole moment compared with that in the T_{MLCT}-**Min** region (50.0 → 70.7 D). These pieces of evidence additionally confirm the occurrence of reductive SET.

Driven by the reductive SET, the C1−C3 bond is gradually elongated (1.533 → 2.000 Å), which has to overcome a medium barrier of **TS-C1C3** (5.5 kcal·mol⁻¹), significantly undermined by the strain of cyclopropane ring[45] and preparatory activation. In this process, the N8−C1 bond undergoes concerted shortening (1.459 → 1.300 Å) in combination with the rotation of the N8−C1 bond (C3C1N8C9 dihedral angle: −24.74 → 21.30°), indicating the partial formation of a N8═C1 double bond. **Int-N8** thus falls into a shallow potential, which increases the detection probability of this intermediate. Once **TS-C1C3** is surpassed, the system proceeds along a downhill path with the complete breaking of the C1−C3 bond (2.000 → 2.394 Å). Meanwhile, the N8═C1 bond is further shortened to 1.291 Å, fully rendered as a double bond, which can also be validated by the coplanarity of C2−C1−C6 and C9−N8−C10 moieties and the evolution of active orbitals. When the strain-driven homolysis of the cyclopropane ring completes, C3 is entirely exposed to get rid of the mutual interactions from the neighboring groups, leading to the generation of a more stable carbon radical **Int-C3** with a slight energy decline (3.0 kcal·mol⁻¹) relative to **Int-N8** (see Figures 3, 4, and S16). The reductive SET-driven

concerted process enables radical migration along the intramolecular π and σ bond networks. As shown in Figure 3B, unpaired electron shifts can be undoubtedly achieved from the visible-light-generated nitrogen-centered radical cation to the carbon-centered radical intermediate. Mulliken population analyses reveal that the excess positive charge on N8 is partly dispersed on the C1−C2−C3 moiety after the electron shift [i.e., N8: **Int-N8** (−0.0296) → **Int-C3** (−0.3054) and C1−C2−C3: **Int-N8** (−0.2369) → **Int-C3** (0.0169)]. Based on these electronic structure calculations, it can be concluded that the radical migration progresses to accomplish the carbon radical formation through the strain-driven homolysis of the cyclopropane ring triggered by the excited-state SET. The high-level quantum-chemical calculations provide comprehensive information on geometric and electronic structure changes during the generation of intermediates, contributing to a better understanding of radical manners, so as to improve and design relevant reactions.

Kinetic Assessment of Multiple Events around Reductive SETs and Analyses and Comparisons of SET Models

To further explore the driving force behind the generation of **Int-C3** from a kinetic perspective, we calculated the rates of various events around the reductive SET. On the basis of the CASPT2//CASSCF/PCM calculated physical parameters shown in Scheme 2A, the reductive SET rate is calculated to be about 1.2×10^7 s⁻¹ in the polar matrix of acetonitrile according to Marcus electron-transfer theory. A key conclusion is that the reductive SET takes place competitively over the phosphorescence emission of photocatalyst **3** from T_{MLCT}-**Min** ($k_p = 7.3 \times 10^4$ s⁻¹) (see Figure 3A). It is a prerequisite of any photosensitized event that the sensitization rate surpasses the emission rate. Based on the energy level of **Int-N8** and **TS-C1C3**, the rate of C1−C3 bond homolysis can be estimated as 6.6×10^8 s⁻¹. Of note, the realistic reaction rate is not confined to this lower bound value since the energy barrier of the transition state is always overestimated compared with the free energy barrier. Therefore, the strain-driven C1−C3 bond homolysis definitely proceeds more efficiently than the reductive SET process definitely. Although relatively accurate free energy calculations are unachievable at the CASPT2//CASSCF level, it can still be concluded that the reductive SET

is the rate-determining step for the entire process. These kinetic calculations reveal that enhancing the reductive SET rate will facilitate the generation of the carbon radical **Int-C3** effectively. Considering the Marcus theory, which emphasizes the potential energy change between two minima in determining electron-transfer rates, improving the stability of critical intermediate **Int-N8** suitably can profoundly accelerate the reductive SET. The above kinetic analyses may contribute to our better understanding of the functions of Lewis acidic salt additives for reaction optimization. For instance, ZnCl₂ can raise the yield of 1-aminoNB **5** from 63 to 84% and even enable partial productivity of **5** when utilizing the less oxidizing photocatalyst Ru(bpy)₃Cl₂ from 0 to 34%.[22c] It is because that Lewis acidic salts can lower the energy of **Int-N8** through modulation of amine oxidation potential (e.g., LiBF₄ can reduce the oxidation peak potential of aminoCP **4** from 1.02 to 0.98 V vs SCE in MeCN) to allow a faster nonadiabatic transition from $T_{MLCT}(^3n\pi^*)$ to $T_{CT}(^3n\pi^*)$, thereby increasing the yields. To sum up, the manipulation of N-centered radical cation **Int-N8** can realize the regulation of this photoredox catalysis in both thermodynamics and kinetics.

Our research group has reported a mechanistic insight for the amide-directed distal sp³ C—H functionalization.[36a] In that work, we demonstrated that the formation of the carbon radical was energetically unfavorable and inefficient via a stepwise path involving PCET (proton-coupled electron transfer) of amide and subsequent 1,5-HAT (hydrogen atom transfer). Then, we proposed an alternative asynchronous concerted mechanism as well as an expanded SET model that combines Marcus electron-transfer theory and transition-state theory. As shown in Scheme 2B, there is not any local minimum between **TS1** and **CI**(T_{MLCT}/T_{21CT}), which means that the catalytic system directly reaches the transition state for HAT after the reductive SET. Based on the energy barrier between **TS1** and T_{MLCT}-**Min**, the rate of the asynchronous concerted HAT process can be estimated as 1.5×10^2 s⁻¹ in a polar solvent of acetonitrile. The stable carbon radical intermediate (**IM1**) emerging after **TS1** is not only the product of HAT but also the outcome of the reductive SET. Therefore, the nonadiabatic transition rate from T_{MLCT} to T_{21CT} can be estimated as 6.9×10^9 s⁻¹. Kinetic calculations evidence that the efficiency of nonadiabatic transition in this case can be accelerated by 2−3 orders of magnitude compared to the oxidation of aminoCP **4**. This is mainly attributed to the formation of the stable carbon radical **IM1**. For the present case, the potential energy from T_{MLCT}-**Min** to **IM1** decreases by 5.0−6.0 kcal·mol⁻¹ (see Scheme 2B), but for the reductive SET of intramolecular (3 + 2)-cycloaddition, the energy increases by around 7.0 kcal·mol⁻¹ (see Scheme 2A). In the expanded SET model, it is explicit that HAT is the rate-determining step; in other words, **TS1** dominates the efficiency for the formation of **IM1**. Seen in this light, the phosphate utilized in the photocatalysis can be interpreted as a "cocatalyst" to effectively bring the barrier of **TS1** down through a concerted bond breaking−formation mechanism, which changes the alkylation of remote C—H bonds from unproductive into high yielding (∼80%). This inference may be further supported by Knowles' quenching experiments, where the phosphate improves the quenching efficiency of amide.[46]

As for the two SET models, sequential model and syncretic model, there are still several similarities and differences that deserve emphasis. First, the discrepancy of rate-determining

steps in the two models primarily arises from the inherent characteristics of photocatalytic reactions themselves. For the intramolecular (3 + 2)-cycloaddition reaction, it is relatively facile to fragment the slightly weak C—C bond of the cyclopropane ring, so SET becomes dominant. However, when it comes to breaking the inert C—H bond (bond energy >100.0 kcal·mol⁻¹),[36b] HAT takes center stage unquestionably. Second, if a local minimum was found between **CI**(T_{MLCT}/T_{CT}) and **TS1** (see the blue dotted line in Scheme 2B), the double-well potential model would degenerate into a classic sequential SET and TS model, in analogy to what is shown in Scheme 2A. Therefore, different electron-transfer models do not have definite boundaries and can be transformed into each other under particular circumstances. Finally, for both models, the energy level of the ground state continuously ascends along the reaction path in the early stage and eventually surpasses the energy curve of T_{CT} until a maximum (∼100.0 kcal·mol⁻¹ for both the models). The extreme rise of the S_0 potential energy curve acts as a functional hindrance to block the formation of carbon radical via a nonradiative transition from T_{CT} to the closed-shell state S_0, i.e., back SET. Fortunately, the efficiency of back SET is just 10^2 to 10^4 s⁻¹ for both the models because of the small nonadiabatic coupling (<1.0 cm⁻¹) at the corresponding singlet−triplet crossing region. It is insufficient to completely intercept the photocatalytic reaction but only slightly lowers the quantum yield. In view of high-accuracy CASPT2//CASSCF/PCM calculations, the rate-determining steps can be predicted without any experimental data support for the excited-state electron-transfer processes, which is hence conducive to accomplishing the regulation of photoredox catalysis. Overall, these insights provide a deeper understanding of the electron-transfer mechanisms and offer guidance for fine-tuning photoredox catalytic reactions.

6-Exo-Trig Cyclization via Radical Addition and 5-Exo-Trig Cyclization Concerted with Oxidation Reaction of the Ir(II) Catalyst

The exposed C3 radical exerts an intense attraction on the intramolecular electron-deficient olefin, leading to an obvious boat conformation formation for **4•+** of **Int-C3** with a shortened C3−C4 distance (3.519 → 2.254 Å) (see Figure 4). These structural reorganizations propel the catalytic system toward a transition-state region by overcoming a moderate energy barrier (**TS-C3C4**: 5.3 kcal·mol⁻¹) (see Figures 3A and S16). Subsequently, a measurable energy drop is observed in both the energy level of S_0 and the reductive $^3n\pi^*$ state with the gradually narrowing energetic splitting between them. This relaxation pathway is structurally characterized by the complete formation of C3−C4 bond (2.254 → 1.654 Å) and the breakage of C4═C7 double bond (1.379 → 1.539 Å). Population analyses reveal that the C3-centered n orbital is gradually converted into the σ orbital between C3 and C4 associated with the collapse of the π orbital of olefin during the C3−C4 bonding process. Moreover, a stable six-membered ring skeleton is constructed in the boat conformation (6-exo-trig), accompanied by the radical migration from the amine-centered C3 radical (**Int-C3**) to the olefin-centered C7 radical (**Int-C7**) (see Figure 3B). Although the six-membered ring in the boat conformation is not as stable as that in the chair conformation, **Int-C7** still tends to adopt the boat conformation since it profits 5-exo-trig cyclization in the subsequent step. Further, TST calculations suggest that this process proceeds at a rate of 7.5×10^8 s⁻¹, 6−7 orders of

magnitude higher than the rate of backward radical inhibition event.

Starting from **Int-C7**, another radical addition happens due to the strong mutual attraction between the C7 radical and the intramolecular electron-poor N8═C1 that formed in the C1─C3 homolysis step. Its barrier is condensed to a tiny value of 1.8 kcal·mol^{-1} because of the preformed boat conformation (see Figures 3A and S16). The energy gap between the energy level of S_0 and T_{CT} is also further narrowed until the second singlet−triplet crossing of $\mathbf{STC(T_{CT}/S_0)}$-**C7C1**, associated with the gradually decreased C7−C1 distance (2.793 → 2.530 Å) and the elongation of the N8═C1 bond (1.294 → 1.315 Å) (see Figure 4). These structural adjustments essentially function as the preparatory steps for the recovery of photocatalyst **3** as well as the production of 1-aminoNB **5**. $\mathbf{STC(T_{CT}/S_0)}$-**C7C1** serves as an energetically allowed relay to pair electrons around the N8 center via the nonadiabatic transition from the open-shell T_{CT} state to the closed-shell ground state (see Figure 3B). Since the Ir photoredox catalyst **3** acts as an electron donor during this radical termination, the electron transfer is identified as oxidative SET. Upon reaching the ground state, the catalytic system rapidly relaxes to the local minimum S_0-**P** for the final product 1-aminoNB **5** along a downhill path with a heat release of 62.5−64.5 kcal·mol^{-1}. This relaxation pathway involves the formation of a C7−C1 bond (2.530 → 1.616 Å) associated with the double-five-membered bridged ring (highlighted with blue and yellow polygons in Figure 4). Careful Mulliken population analyses reveal that the excess negative charge of the reduced Ir photocatalyst is transferred back to N8 and other parts of final product **5** after the oxidative SET [i.e., Ir-dtbbpy: **Int-C7** (−0.0732) → S_0-**P** (0.6939) and N8: **Int-C7** (−0.3617) → S_0-**P** (−0.6944)], indicating the regeneration of photocatalyst **3** (see Table S6). As shown in Scheme S1, the oxidative SET is more effective than the previous reductive SET (estimated as 1.1×10^{10} s^{-1}) owing to an amount of heat release (>60.0 kcal·mol^{-1}). For this whole photoredox catalysis, the reductive SET is still the rate-determining step.

CONCLUSIONS

In this study, we conducted comprehensive mechanistic research into the intramolecular photo-(3 + 2)-cycloaddition reactions of imine and amine substrates using high-precision CASPT2//CASSCF/PCM calculations. Our findings reveal that the imine substrates can directly harness visible light for initiation, thanks to their unique n → π* transition, whereas the amine substrates require the sensitization by the photocatalyst due to the absence of conjugated moieties. The native strain of the cyclopropane ring plays a crucial role in lowering the C−C homolysis barrier. The barrier virtually vanishes for the imine system, but the amine system still exhibits a moderate barrier. This discrepancy can be attributed to the smaller structural adjustment of imine substrates during the homolysis process, leading to a more favorable reaction pathway for them. Thus, the masked N-centered radical presents a higher reactivity than the N-centered radical cation. The irreversible 6-exo-trig and 5-exo-trig cyclizations serve as the radical propagation procedures, with the 5-exo-trig cyclization coinciding with the radical termination. The reaction of the imine system does not involve changes in the spin multiplicity, highlighting the barriers on the adiabatic states in regulating the reaction. However, the fast internal conversion between different states with identical spin multiplicity severely diminishes the quantum efficiency of this photoreaction, potentially imposing limitations on its further application. Regarding the photoredox catalytic system, the reaction predominantly takes place on the triplet states owing to strong relativistic effects of the Ir atom, thereby primarily tuned by the transitions between different states, especially SETs. The limited quantum yield of the photocatalyst itself and the occurrence of back SET are the main factors impeding the quantum efficiency. This difficulty may be addressed by a new high-efficiency catalyst design based on high-precision theoretical calculations.

Meanwhile, our analysis and comparison of two representative SET models provide a thorough understanding of their characteristics as well as their similarities and differences. By recognizing the distinct features of various photoredox catalyzes, we can employ the corresponding models associated with the high-precision quantum-chemical calculations to effectively achieve the fine-tuning of reactions. These models are also further enrichment and improvement of Marcus electron-transfer theory and the transition-state theory, which facilitate our enhanced comprehension of electron-transfer phenomena. Our research group will always be devoted to developing more SET models.[47] In general, these theoretical advancements hold promising prospects for the mechanism-guided molecular design of photocatalysts and the photochemical synthetic method design of new building blocks, especially saturated blocks suitable for pharmaceutical chemistry.

■ ASSOCIATED CONTENT

Ⓢ Supporting Information

The Supporting Information is available free of charge at https://pubs.acs.org/doi/10.1021/jacsau.3c00542.

> Computational details on CASPT2//CASSCF, calculations of vertical excitation and adiabatic excitation for substrates and photocatalysts, phosphorescence lifetime calculations, redox potential calculations, rate constant calculations, charge translocation calculations, population analyses, conformational analyses, other possible reaction paths, single-point energies, Cartesian coordinates, and additional references (PDF)

■ AUTHOR INFORMATION

Corresponding Author

Xuebo Chen − *College of Chemistry, Beijing Normal University, Beijing 100875, People's Republic of China;* ⓞ orcid.org/0000-0002-9814-9908; Email: xuebochen@bnu.edu.cn

Authors

Chu Wang − *College of Chemistry, Beijing Normal University, Beijing 100875, People's Republic of China*

Xiao Liu − *College of Chemistry, Beijing Normal University, Beijing 100875, People's Republic of China*

Qian Wang − *College of Chemistry, Beijing Normal University, Beijing 100875, People's Republic of China*

Wei-Hai Fang − *College of Chemistry, Beijing Normal University, Beijing 100875, People's Republic of China;* ⓞ orcid.org/0000-0002-1668-465X

Complete contact information is available at:
https://pubs.acs.org/10.1021/jacsau.3c00542

REFERENCES

(1) (a) Meanwell, N. A. Improving Drug Design: An Update on Recent Applications of Efficiency Metrics, Strategies for Replacing Problematic Elements, and Compounds in Nontraditional Drug Space. *Chem. Res. Toxicol.* **2016**, *29*, 564−616. (b) Ritchie, T. J.; Macdonald, S. J. F. Physicochemical Descriptors of Aromatic Character and Their Use in Drug Discovery. *J. Med. Chem.* **2014**, *57*, 7206−7215. (c) Lovering, F.; Bikker, J.; Humblet, C. Escape from Flatland: Increasing Saturation as an Approach to Improving Clinical Success. *J. Med. Chem.* **2009**, *52*, 6752−6756.

(2) Subbaiah, M. A. M.; Meanwell, N. A. Bioisosteres of the Phenyl Ring: Recent Strategic Applications in Lead Optimization and Drug Design. *J. Med. Chem.* **2021**, *64*, 14046−14128.

(3) Shearer, J.; Castro, J. L.; Lawson, A. D. G.; MacCoss, M.; Taylor, R. D. Rings in Clinical Trials and Drugs: Present and Future. *J. Med. Chem.* **2022**, *65*, 8699−8712.

(4) (a) Locke, G. M.; Bernhard, S. S. R.; Senge, M. O. Nonconjugated Hydrocarbons as Rigid-Linear Motifs: Isosteres for Material Sciences and Bioorganic and Medicinal Chemistry. *Chem.—Eur. J.* **2019**, *25*, 4590−4647. (b) Stockdale, T. P.; Williams, C. M. Pharmaceuticals that Contain Polycyclic Hydrocarbon Scaffolds. *Chem. Soc. Rev.* **2015**, *44*, 7737−7763. (c) Ritchie, T. J.; Macdonald, S. J. F.; Young, R. J.; Pickett, S. D. The Impact of Aromatic Ring Count on Compound Developability: Further Insights by Examining Carbo- and Hetero-Aromatic and -Aliphatic Ring Types. *Drug Discovery Today* **2011**, *16*, 164−171.

(5) Kalgutkar, A. S.; Dalvie, D. Predicting Toxicities of Reactive Metabolite−Positive Drug Candidates. *Annu. Rev. Pharmacol. Toxicol.* **2015**, *55*, 35−54.

(6) (a) Beak, P. Silver-Assisted Reactions of Chloroformates: A New Route to Reactive Carbocations. *Acc. Chem. Res.* **1976**, *9*, 230−236. (b) Applequist, D. E.; Roberts, J. D. Displacement Reactions at Bridgeheads of Bridged Polycarbocyclic Systems. *Chem. Rev.* **1954**, *54*, 1065−1089. (c) Bartlett, P. D.; Knox, L. H. Bicyclic Structures Prohibiting the Walden Inversion. Replacement Reactions in 1-Substituted 1-Apocamphanes. *J. Am. Chem. Soc.* **1939**, *61*, 3184−3192.

(7) (a) Dejmek, M.; Hřebabecký, H.; Sala, M.; Dračínský, M.; Prochazkova, E.; Leyssen, P.; Neyts, J.; Balzarini, J.; Nencka, R. From Norbornane-Based Nucleotide Analogs Locked in South Conformation to Novel Inhibitors of Feline Herpes Virus. *Bioorg. Med. Chem.* **2014**, *22*, 2974−2983. (b) Buser, S.; Vasella, A. 7-Oxanorbornane and Norbornane Mimics of a Distorted β-D-Mannopyranoside: Synthesis and Evaluation as β-Mannosidase Inhibitors. *Helv. Chim. Acta* **2005**, *88*, 3151−3173. (c) Nickon, A.; Nishida, T.; Lin, Y.-I. Bridgehead Ketols. *J. Am. Chem. Soc.* **1969**, *91*, 6860−6861. (d) Wilt, J. W.; Parsons, C. T.; Schneider, C. A.; Schultenover, D. G.; Wagner, W. J. Preparation and study of some 1-norbornenyl and norbornenyl-1-carbinyl derivatives. *J. Org. Chem.* **1968**, *33*, 694−708.

(8) (a) Kitcatt, D. M.; Nicolle, S.; Lee, A.-L. Direct Decarboxylative Giese Reactions. *Chem. Soc. Rev.* **2022**, *51*, 1415−1453. (b) Gilmore, K.; Alabugin, I. V. Cyclizations of Alkynes: Revisiting Baldwin's Rules for Ring Closure. *Chem. Rev.* **2011**, *111*, 6513−6556. (c) Zhang, W. Intramolecular free radical conjugate additions. *Tetrahedron* **2001**, *57*, 7237−7262.

(9) (a) Della, E. W.; Kostakis, C.; Smith, P. A. Regioselective 6-Endo Cyclization of 5-Carbomethoxy-5-hexenyl Radicals: A Convenient Synthesis of Derivatives of the 1-Azabicyclo[2.2.1]heptyl System. *Org. Lett.* **1999**, *1*, 363−366. (b) Della, E. W.; Knill, A. M.; Smith, P. A. Novel synthesis of bridgehead nitrogen heterocycles by ring-closure of

α-ammonio radicals. *Chem. Commun.* **1996**, 1637−1638. (c) Della, E. W.; Knill, A. M. Synthesis of Bridgehead Substituted Bicyclo[2.2.1]-Heptanes. Radical Cyclization of an Oxime Ether and an α,β-Unsaturated Ester. *Aust. J. Chem.* **1994**, *47*, 1833−1841.

(10) (a) Chan, A. Y.; Perry, I. B.; Bissonnette, N. B.; Buksh, B. F.; Edwards, G. A.; Frye, L. I.; Garry, O. L.; Lavagnino, M. N.; Li, B. X.; Liang, Y.; Mao, E.; Millet, A.; Oakley, J. V.; Reed, N. L.; Sakai, H. A.; Seath, C. P.; MacMillan, D. W. C. Metallaphotoredox: The Merger of Photoredox and Transition Metal Catalysis. *Chem. Rev.* **2022**, *122*, 1485−1542. (b) Twilton, J.; Le, C.; Zhang, P.; Shaw, M. H.; Evans, R. W.; MacMillan, D. W. C. The Merger of Transition Metal and Photocatalysis. *Nat. Rev. Chem* **2017**, *1*, 0052. (c) Shaw, M.; Twilton, J.; MacMillan, D. W. C. Photoredox Catalysis in Organic Chemistry. *J. Org. Chem.* **2016**, *81*, 6898−6926. (d) Prier, C. K.; Rankic, D. A.; MacMillan, D. W. C. Visible Light Photoredox Catalysis with Transition Metal Complexes: Applications in Organic Synthesis. *Chem. Rev.* **2013**, *113*, 5322−5363.

(11) (a) Liu, W.; Lavagnino, M. N.; Gould, C. A.; Alcázar, J.; MacMillan, D. W. C. A Biomimetic S_H2 Cross-Coupling Mechanism for Quaternary sp^3-Carbon Formation. *Science* **2021**, *374*, 1258−1263. (b) Geri, J. B.; Oakley, J. V.; Reyes-Robles, T.; Wang, T.; McCarver, S. J.; White, C. H.; Rodriguez-Rivera, F. P.; Parker, D. L., Jr.; Hett, E. C.; Fadeyi, O. O.; Oslund, R. C.; MacMillan, D. W. C. Microenvironment Mapping via Dexter Energy Transfer on Immune Cells. *Science* **2020**, *367*, 1091−1097. (c) DeHovitz, J. S.; Loh, Y. Y.; Kautzky, J. A.; Nagao, K.; Meichan, A. J.; Yamauchi, M.; MacMillan, D. W. C.; Hyster, T. K. Static to Inducibly Dynamic Stereocontrol: The Convergent Use of Racemic β-Substituted Ketones. *Science* **2020**, *369*, 1113−1118. (d) Lovett, G. H.; Chen, S.; Xue, X.-S.; Houk, K. N.; MacMillan, D. W. C. Open-Shell Fluorination of Alkyl Bromides: Unexpected Selectivity in a Silyl Radical-Mediated Chain Process. *J. Am. Chem. Soc.* **2019**, *141*, 20031−20036. (e) Nacsa, E. D.; MacMillan, D. W. C. Spin-Center Shift-Enabled Direct Enantioselective α-Benzylation of Aldehydes with Alcohols. *J. Am. Chem. Soc.* **2018**, *140*, 3322−3330. (f) Capacci, A. G.; Malinowski, J. T.; McAlpine, N. J.; Kuhne, J.; MacMillan, D. W. C. Direct, enantioselective α-alkylation of aldehydes using simple olefins. *Nat. Chem.* **2017**, *9*, 1073−1077.

(12) (a) Jin, J.; MacMillan, D. W. C. Alcohols as Alkylating Agents in Heteroarene CH Functionalization. *Nature* **2015**, *525*, 87−90. (b) Jin, J.; MacMillan, D. W. C. Direct α-Arylation of Ethers through the Combination of Photoredox-Mediated C−H Functionalization and the Minisci Reaction. *Angew. Chem., Int. Ed.* **2015**, *54*, 1565−1569. (c) Jeffrey, J. L.; Petronijević, F. R.; MacMillan, D. W. C. Selective Radical−Radical Cross-Couplings: Design of a Formal β-Mannich Reaction. *J. Am. Chem. Soc.* **2015**, *137*, 8404−8407. (d) Cuthbertson, J. D.; MacMillan, D. W. C. The Direct Arylation of Allylic sp^3 C−H Bonds via Organic and Photoredox Catalysis. *Natures* **2015**, *519*, 74−77.

(13) (a) Noble, A.; Macmillan, D. W. C. Photoredox α-Vinylation of α-Amino Acids and N-Aryl Amines. *J. Am. Chem. Soc.* **2014**, *136*, 11602−11605. (b) Hager, D.; MacMillan, D. W. C. Activation of C−H Bonds via the Merger of Photoredox and Organocatalysis: A Coupling of Benzylic Ethers with Schiff Bases. *J. Am. Chem. Soc.* **2014**, *136*, 16986−16989. (c) Chu, L.; Ohta, C.; Zuo, Z.; MacMillan, D. W. C. Carboxylic Acids as A Traceless Activation Group for Conjugate Additions: A Three-Step Synthesis of (±)-Pregabalin. *J. Am. Chem. Soc.* **2014**, *136*, 10886−10889. (d) Zuo, Z.; MacMillan, D. W. C. Decarboxylative Arylation of α-Amino Acids via Photoredox Catalysis: A One-Step Conversion of Biomass to Drug Pharmacophore. *J. Am. Chem. Soc.* **2014**, *136*, 5257−5260. (e) Terrett, J. A.; Clift, M. D.; MacMillan, D. W. C. Direct β-Alkylation of Aldehydes via Photoredox Organocatalysis. *J. Am. Chem. Soc.* **2014**, *136*, 6858−6861. (f) Qvortrup, K.; Rankic, D. A.; MacMillan, D. W. C. A General Strategy for Organocatalytic Activation of C−H Bonds via Photoredox Catalysis: Direct Arylation of Benzylic Ethers. *J. Am. Chem. Soc.* **2014**, *136*, 626−629.

(14) (a) Pirnot, M. T.; Rankic, D. A.; Martin, D. B. C.; MacMillan, D. W. C. Photoredox Activation for the Direct β-Arylation of Ketones

and Aldehydes. *Science* **2013**, *339*, 1593−1596. (b) Petronijević, F. R.; Nappi, M.; MacMillan, D. W. C. Direct β-Functionalization of Cyclic Ketones with Aryl Ketones via the Merger of Photoredox and Organocatalysis. *J. Am. Chem. Soc.* **2013**, *135*, 18323−18326. (c) McNally, A.; Prier, C. K.; MacMillan, D. W. C. Discovery of an α-Amino C−H Arylation Reaction Using the Strategy of Accelerated Serendipity. *Science* **2011**, *334*, 1114−1117. (d) Nicewicz, D. A.; MacMillan, D. W. C. Merging Photoredox Catalysis with Organocatalysis: The Direct Asymmetric Alkylation of Aldehydes. *Science* **2008**, *322*, 77−80.

(15) (a) Dow, N. W.; Cabré, A.; MacMillan, D. W. C. A General N-alkylation Platform via Copper Metallaphotoredox and Silyl Radical Activation of Alkyl Halides. *Chem* **2021**, *7*, 1827−1842. (b) Zhang, X.; Smith, R. T.; Le, C.; McCarver, S. J.; Shireman, B. T.; Carruthers, N. I.; MacMillan, D. W. C. Copper-Mediated Synthesis of Drug-Like Bicyclopentanes. *Nature* **2020**, *580*, 220−226. (c) Sarver, P. J.; Bacauanu, V.; Schultz, D. M.; DiRocco, D. A.; Lam, Y.-H.; Sherer, E. C.; MacMillan, D. W. C. The Merger of Decatungstate and Copper Catalysis to Enable Aliphatic C(sp^3) − H Trifluoromethylation. *Nat. Chem.* **2020**, *12*, 459−467. (d) Kautzky, J. A.; Wang, T.; Evans, R. W.; MacMillan, D. W. C. Decarboxylative Trifluoromethylation of Aliphatic Carboxylic Acids. *J. Am. Chem. Soc.* **2018**, *140*, 6522−6526. (e) Kornfilt, D. J. P.; MacMillan, D. W. C. Copper-Catalyzed Trifluoromethylation of Alkyl Bromides. *J. Am. Chem. Soc.* **2019**, *141*, 6853−6858. (f) Le, C.; Chen, T. Q.; Liang, T.; Zhang, P.; MacMillan, D. W. C. A Radical Approach to the Copper Oxidative Addition Problem: Trifluoromethylation of Bromoarenes. *Science* **2018**, *360*, 1010−1014.

(16) (a) Sakai, H. A.; MacMillan, D. W. C. Nontraditional Fragment Couplings of Alcohols and Carboxylic Acids: C(sp^3)−C(sp^3) Cross-Coupling via Radical Sorting. *J. Am. Chem. Soc.* **2022**, *144*, 6185−6192. (b) Dong, Z.; MacMillan, D. W. C. Metallaphotoredox-Enabled Deoxygenative arylation of Alcohols. *Nature* **2021**, *598*, 451−456. (c) Kim, T.; McCarver, S. J.; Lee, C.; MacMillan, D. W. C. Sulfonamidation of Aryl and Heteroaryl Halides through Photosensitized Nickel Catalysis. *Angew. Chem., Int. Ed.* **2018**, *57*, 3488−3492. (d) Till, N. A.; Smith, R. T.; MacMillan, D. W. C. Decarboxylative Hydroalkylation of Alkynes. *J. Am. Chem. Soc.* **2018**, *140*, 5701−5705. (e) Sakai, H. A.; Liu, W.; Le, C.; MacMillan, D. W. C. Cross-Electrophile Coupling of Unactivated Alkyl Chlorides. *J. Am. Chem. Soc.* **2020**, *142*, 11691−11697. (f) Twilton, J.; Christensen, M.; DiRocco, D. A.; Ruck, R. T.; Davies, I. W.; MacMillan, D. W. C. Selective Hydrogen Atom Abstraction through Induced Bond Polarization: Direct α-Arylation of Alcohols through Photoredox, HAT, and Nickel Catalysis. *Angew. Chem., Int. Ed.* **2018**, *57*, 5369−5373.

(17) (a) Le, C.; Liang, Y.; Evans, R. W.; Li, X.; MacMillan, D. W. C. Selective sp^3 C−H Alkylation via Polarity-Matchbased Cross-Coupling. *Nature* **2017**, *547*, 79−83. (b) Zhang, X.; MacMillan, D. W. C. Direct Aldehyde C−H Arylation and Alkylation via the Combination of Nickel, Hydrogen Atom Transfer, and Photoredox Catalysis. *J. Am. Chem. Soc.* **2017**, *139*, 11353−11356. (c) Corcoran, E. B.; Pirnot, M. T.; Lin, S.; Dreher, S. D.; DiRocco, D. A.; Davies, I. W.; Buchwald, S. L.; MacMillan, D. W. C. Aryl Amination Using Ligand-Free Ni(II) Salts and Photoredox Catalysis. *Science* **2016**, *353*, 279−283. (d) Johnston, C. P.; Smith, R. T.; Allmendinger, S.; MacMillan, D. W. C. Metallaphotoredox-Catalysed sp^3−sp^3 Cross-Coupling of Carboxylic Acids with Alkyl Halides. *Nature* **2016**, *536*, 322−325. (e) Terrett, J. A.; Cuthbertson, J. D.; Shurtleff, V. W.; MacMillan, D. W. C. Switching on Elusive Organometallic Mechanisms with Photoredox Catalysis. *Nature* **2015**, *524*, 330−334. (f) Zuo, Z.; Ahneman, D. T.; Chu, L.; Terrett, J. A.; Doyle, A. G.; MacMillan, D. W. C. Merging Photoredox with Nickel Catalysis: Coupling of α-Carboxyl sp^3-Carbons with Aryl Halides. *Science* **2014**, *345*, 437−440.

(18) (a) Reed, N. L.; Yoon, T. P. Oxidase Reactions in Photoredox Catalysis. *Chem. Soc. Rev.* **2021**, *50*, 2954−2967. (b) Yoon, T. P. Stereocontrolled Photochemical Synthesis. *ChemPhotoChem.* **2019**, *3*, 1201−1202. (c) Skubi, K. L.; Blum, T. R.; Yoon, T. P. Dual Catalysis

Strategies in Photochemical Synthesis. *Chem. Rev.* **2016**, *116*, 10035−10074. (d) Yoon, T. P. Photochemical Stereocontrol Using Tandem Photoredox−Chiral Lewis Acid Catalysis. *Acc. Chem. Res.* **2016**, *49*, 2307−2315. (e) Schultz, D. M.; Yoon, T. P. Solar Synthesis: Prospects in Visible Light Photocatalysis. *Science* **2014**, *343*, 1239176.

(19) (a) Li, Q. Y.; Gockel, S. N.; Lutovsky, G. A.; DeGlopper, K. S.; Baldwin, N. J.; Bundesmann, M. W.; Tucker, J. W.; Bagley, S. W.; Yoon, T. P. Decarboxylative Cross-Nucleophile Coupling via Ligand-to-Metal Charge Transfer Photoexcitation of Cu(II) Carboxylates. *Nat. Chem.* **2022**, *14*, 94−99. (b) Farney, E. P.; Chapman, S. J.; Swords, W. B.; Torelli, M. D.; Hamers, R. J.; Yoon, T. P. Discovery and Elucidation of Counteranion Dependence in Photoredox Catalysis. *J. Am. Chem. Soc.* **2019**, *141*, 6385−6391. (c) Zheng, J.; Swords, W. B.; Jung, H.; Skubi, K. L.; Kidd, J. B.; Meyer, G. J.; Baik, M.-H.; Yoon, T. P. Enantioselective Intermolecular Excited-State Photoreactions Using a Chiral Ir Triplet Sensitizer: Separating Association from Energy Transfer in Asymmetric Photocatalysis. *J. Am. Chem. Soc.* **2019**, *141*, 13625−13634. (d) Blum, T. R.; Miller, Z. D.; Bates, D. M.; Guzei, I. A.; Yoon, T. P. Enantioselective Photochemistry through Lewis Acid-Catalyzed Triplet Energy Transfer. *Science* **2016**, *354*, 1391−1395. (e) Scholz, S. O.; Farney, E. P.; Kim, S.; Bates, D. M.; Yoon, T. P. Spin-Selective Generation of Triplet Nitrenes: Olefin Aziridination through Visible-Light Photosensitization of Azidoformates. *Angew. Chem., Int. Ed.* **2016**, *55*, 2239−2242.

(20) Ischay, M. A.; Anzovino, M. E.; Du, J.; Yoon, T. P. Efficient Visible Light Photocatalysis of [2 + 2] Enone Cycloadditions. *J. Am. Chem. Soc.* **2008**, *130*, 12886−12887.

(21) (a) Allen, A. R.; Noten, E. A.; Stephenson, C. R. J. Aryl Transfer Strategies Mediated by Photoinduced Electron Transfer. *Chem. Rev.* **2022**, *122*, 2695−2751. (b) McAtee, R. C.; McClain, E. J.; Stephenson, C. R. J. Illuminating Photoredox Catalysis. *Trends Chem.* **2019**, *1*, 111−125. (c) Kärkäs, M. D.; Porco, J. A., Jr.; Stephenson, C. R. J. Photochemical Approaches to Complex Chemotypes: Applications in Natural Product Synthesis. *Chem. Rev.* **2016**, *116*, 9683−9747. (d) Staveness, D.; Bosque, I.; Stephenson, C. R. J. Free Radical Chemistry Enabled by Visible Light-Induced Electron Transfer. *Acc. Chem. Res.* **2016**, *49*, 2295−2306. (e) Douglas, J. J.; Sevrin, M. J.; Stephenson, C. R. J. Visible Light Photocatalysis: Applications and New Disconnections in the Synthesis of Pharmaceutical Agents. *Org. Process Res. Dev.* **2016**, *20*, 1134−1147.

(22) (a) Harmata, A. S.; Spiller, T. E.; Sowden, M. J.; Stephenson, C. R. J. Photochemical Formal (4 + 2)-Cycloaddition of Imine-Substituted Bicyclo[1.1.1]pentanes and Alkenes. *J. Am. Chem. Soc.* **2021**, *143*, 21223−21228. (b) Staveness, D.; Collins, J. L.; McAtee, R. C.; Stephenson, C. R. J. Exploiting Imine Photochemistry for Masked N-Centered Radical Reactivity. *Angew. Chem., Int. Ed.* **2019**, *58*, 19000−19006. (c) Staveness, D.; Sodano, T. M.; Li, K.; Burnham, E. A.; Jackson, K. D.; Stephenson, C. R. J. Providing a New Aniline Bioisostere through the Photochemical Production of 1-Amino-norbornanes. *Chem* **2019**, *5*, 215−226. (d) Collins, J. L.; Staveness, D.; Sowden, M. J.; Stephenson, C. R. J. A One-Pot Photochemical Method for the Generation of Functionalized Aminocyclopentanes. *Org. Lett.* **2022**, *24*, 4344−4348.

(23) (a) McClain, E. J.; Monos, T. M.; Mori, M.; Beatty, J. W.; Stephenson, C. R. J. Design and Implementation of a Catalytic Electron Donor−Acceptor Complex Platform for Radical Trifluoromethylation and Alkylation. *ACS Catal.* **2020**, *10*, 12636−12641. (b) McAtee, R. C.; Noten, E. A.; Stephenson, C. R. J. Arene Dearomatization through a Catalytic N-centered Radical Cascade Reaction. *Nat. Commun.* **2020**, *11*, 2528. (c) Monos, T. M.; McAtee, R. C.; Stephenson, C. R. J. Arylsulfonylacetamides as Bifunctional Reagents for Alkene Aminoarylation. *Science* **2018**, *361*, 1369−1373.

(24) Narayanam, J. M. R.; Tucker, J. W.; Stephenson, C. R. J. Electron-Transfer Photoredox Catalysis: Development of a Tin-Free Reductive Dehalogenation Reaction. *J. Am. Chem. Soc.* **2009**, *131*, 8756−8757.

(25) (a) Lu, F.-D.; Chen, J.; Jiang, X.; Chen, J.-R.; Lu, L.-Q.; Xiao, W.-J. Recent Advances in Transition-Metal-Catalysed Asymmetric

Coupling Reactions with Light Intervention. *Chem. Soc. Rev.* **2021**, *50*, 12808−12827. (b) Yu, X.-Y.; Chen, J.-R.; Xiao, W.-J. Visible Light-Driven Radical-Mediated C−C Bond Cleavage/Functionalization in Organic Synthesis. *Chem. Rev.* **2021**, *121*, 506−561. (c) Pramanik, M. M. D.; Qian, H.; Xiao, W.-J.; Chen, J.-R. Photoinduced Strategies towards Strained Molecules. *Org. Chem. Front.* **2020**, *7*, 2531−2537. (d) Yu, X.-Y.; Zhao, Q.-Q.; Chen, J.; Xiao, W.-J.; Chen, J.-R. When Light Meets Nitrogen-Centered Radicals: From Reagents to Catalysts. *Acc. Chem. Res.* **2020**, *53*, 1066−1083.

(26) Romero, N. A.; Nicewicz, D. A. Organic Photoredox Catalysis. *Chem. Rev.* **2016**, *116*, 10075−10166.

(27) Jamison, C. R.; Overman, L. E. Fragment Coupling with Tertiary Radicals Generated by Visible-Light Photocatalysis. *Acc. Chem. Res.* **2016**, *49*, 1578−1586.

(28) Nakajima, K.; Miyake, Y.; Nishibayashi, Y. Synthetic Utilization of α-Aminoalkyl Radicals and Related Species in Visible Light Photoredox Catalysis. *Acc. Chem. Res.* **2016**, *49*, 1946−1956.

(29) (a) Strieth-Kalthoff, F.; James, M. J.; Teders, M.; Pitzer, L.; Glorius, F. Energy Transfer Catalysis Mediated by Visible Light: Principles, Applications, Directions. *Chem. Soc. Rev.* **2018**, *47*, 7190−7202. (b) Hopkinson, M. N.; Tlahuext-Aca, A.; Glorius, F. Merging Visible Light Photoredox and Gold Catalysis. *Acc. Chem. Res.* **2016**, *49*, 2261−2272. (c) Sahoo, B.; Hopkinson, M. N.; Glorius, F. Combining Gold and Photoredox Catalysis: Visible Light-Mediated Oxy- and Aminoarylation of Alkenes. *J. Am. Chem. Soc.* **2013**, *135*, 5505−5508.

(30) He, Z.; Bae, M.; Wu, J.; Jamison, T. F. Synthesis of Highly Functionalized Polycyclic Quinoxaline Derivatives Using Visible-Light Photoredox Catalysis. *Angew. Chem., Int. Ed.* **2014**, *53*, 14451−14455.

(31) Das, S.; Zhu, C.; Demirbas, D.; Bill, E.; De, C. K.; List, B. Asymmetric Counteranion-Directed Photoredox Catalysis. *Science* **2023**, *379*, 494−499.

(32) Ohmura, S.; Katagiri, K.; Kato, H.; Horibe, T.; Miyakawa, S.; Hasegawa, J.; Ishihara, K. Highly Enantioselective Radical Cation [2 + 2] and [4 + 2] Cycloadditions by Chiral Iron(III) Photoredox Catalysis. *J. Am. Chem. Soc.* **2023**, *145*, 15054−15060.

(33) Latrache, M.; Hoffmann, N. Photochemical Radical Cyclization Reactions with Imines, Hydrazones, Oximes and Related Compounds. *Chem. Soc. Rev.* **2021**, *50*, 7418−7435.

(34) (a) Limburg, B.; Cristòfol, À.; Kleij, A. W. Decoding Key Transient Inter-Catalyst Interactions in a Reductive Metallaphotoredox-Catalyzed Allylation Reaction. *J. Am. Chem. Soc.* **2022**, *144*, 10912−10920. (b) Cagan, D. A.; Bím, D.; Silva, B.; Kazmierczak, N. P.; McNicholas, B. J.; Hadt, R. G. Elucidating the Mechanism of Excited-State Bond Homolysis in Nickel−Bipyridine Photoredox Catalysts. *J. Am. Chem. Soc.* **2022**, *144*, 6516−6531. (c) Qin, Y.; Zhu, Q.; Sun, R.; Ganley, J. M.; Knowles, R. R.; Nocera, D. G. Mechanistic Investigation and Optimization of Photoredox Anti-Markovnikov Hydroamination. *J. Am. Chem. Soc.* **2021**, *143*, 10232−10242. (d) Qin, Y.; Sun, R.; Gianoulis, N. P.; Nocera, D. G. Photoredox Nickel-Catalyzed C−S Cross-Coupling: Mechanism, Kinetics, and Generalization. *J. Am. Chem. Soc.* **2021**, *143*, 2005−2015. (e) Till, N. A.; Tian, L.; Dong, Z.; Scholes, G. D.; MacMillan, D. W. C. Mechanistic Analysis of Metallaphotoredox C−N Coupling: Photocatalysis Initiates and Perpetuates Ni(I)/Ni(III) Coupling Activity. *J. Am. Chem. Soc.* **2020**, *142*, 15830−15841. (f) Tian, L.; Till, N. A.; Kudisch, B.; MacMillan, D. W. C.; Scholes, G. D. Transient Absorption Spectroscopy Offers Mechanistic Insights for an Iridium/Nickel-Catalyzed C−O Coupling. *J. Am. Chem. Soc.* **2020**, *142*, 4555−4559.

(35) (a) Studer, A.; Curran, D. P. Catalysis of Radical Reactions: A Radical Chemistry Perspective. *Angew. Chem., Int. Ed.* **2016**, *55*, 58−102. (b) Chatgilialoglu, C.; Studer, A. *Encyclopedia of Radicals in Chemistry, Biology and Materials*; Wiley: Chichester, 2012; pp 147−174. (c) Hogg, N. Detection of Nitric Oxide by Electron Paramagnetic Resonance Spectroscopy. *Free Radical Biol. Med.* **2010**, *49*, 122−129.

(36) (a) Wang, J.; Fang, W.-H.; Qu, L.-B.; Shen, L.; Maseras, F.; Chen, X. An Expanded SET Model Associated with the Functional

Hindrance Dominates the Amide-Directed Distal sp^3 C−H Functionalization. *J. Am. Chem. Soc.* **2021**, *143*, 19406−19416. (b) Yang, W.; Chen, X.; Fang, W.-H. Nonadiabatic Curve-Crossing Model for the Visible-Light Photoredox Catalytic Generation of Radical Intermediate via a Concerted Mechanism. *ACS Catal.* **2018**, *8*, 7388−7396. (c) Liu, H.; Ma, L.; Zhou, R.; Chen, X.; Fang, W.-H.; Wu, J. One-Pot Photomediated Giese Reaction/Friedel−Crafts Hydroxyalkylation/Oxidative Aromatization To Access Naphthalene Derivatives from Toluenes and Enones. *ACS Catal.* **2018**, *8*, 6224−6229. (d) Wu, L.; Cao, X.; Chen, X.; Fang, W.-H.; Dolg, M. Visible-Light Photocatalysis of C(sp^3)-H Fluorination by the Uranyl Ion: Mechanistic Insights. *Angew. Chem., Int. Ed.* **2018**, *57*, 11812−11816. (e) Wang, H.; Cao, X.; Chen, X.; Fang, W.-H.; Dolg, M. Regulatory Mechanism of the Enantioselective Intramolecular Enone [2 + 2] Photocycloaddition Reaction Mediated by a Chiral Lewis Acid Catalyst Containing Heavy Atoms. *Angew. Chem., Int. Ed.* **2015**, *54*, 14295−14298.

(37) (a) Kwon, K.; Simons, R. T.; Nandakumar, M.; Roizen, J. L. Strategies to Generate Nitrogen-centered Radicals That May Rely on Photoredox Catalysis: Development in Reaction Methodology and Applications in Organic Synthesis. *Chem. Rev.* **2022**, *122*, 2353−2428. (b) Kärkäs, M. D. Photochemical Generation of Nitrogen-Centered Amidyl, Hydrazonyl, and Imidyl Radicals: Methodology Developments and Catalytic Applications. *ACS Catal.* **2017**, *7*, 4999−5022.

(38) Ma, L.; Fang, W.-H.; Shen, L.; Chen, X. Regulatory Mechanism and Kinetic Assessment of Energy Transfer Catalysis Mediated by Visible Light. *ACS Catal.* **2019**, *9*, 3672−3684.

(39) Karafiloglou, P.; Harcourt, R. D. Aspects of Three-Electron Two-Centre, Four-Electron Three-Centre and Six-Electron Five-Centre bonding in cycloimmonium ylides. *J. Mol. Struct.: THEOCHEM* **2005**, *729*, 155−161.

(40) Lowry, M. S.; Goldsmith, J. I.; Slinker, J. D.; Rohl, R.; Pascal, R. A.; Malliaras, G. G.; Bernhard, S. Single-Layer Electroluminescent Devices and Photoinduced Hydrogen Production from an Ionic Iridium(III) Complex. *Chem. Mater.* **2005**, *17*, 5712−5719.

(41) Bokarev, S. I.; Bokareva, O. S.; Kühn, O. Electronic Excitation Spectrum of the Photosensitizer $[Ir(ppy)_2(bpy)]^+$. *J. Chem. Phys.* **2012**, *136*, 214305.

(42) (a) Improta, R.; Santoro, F.; Blancafort, L. Quantum Mechanical Studies on the Photophysics and the Photochemistry of Nucleic Acids and Nucleobases. *Chem. Rev.* **2016**, *116*, 3540−3593. (b) Andersson, K.; Malmqvist, P. Å.; Roos, B. O.; Sadlej, A. J.; Wolinski, K. Second-Order Perturbation Theory with a CASSCF Reference Function. *J. Phys. Chem.* **1990**, *94*, 5483−5488. (c) Andersson, K.; Malmqvist, P. Å.; Roos, B. O. Second-Order Perturbation Theory with a Complete Active Space Self-Consistent Field Reference Function. *J. Chem. Phys.* **1992**, *96*, 1218−1226.

(43) Duan, Y.-C.; Wen, L.-L.; Gao, Y.; Wu, Y.; Zhao, L.; Geng, Y.; Shan, G.-G.; Zhang, M.; Su, Z.-M. Fluorescence, Phosphorescence, or Delayed Fluorescence?— A Theoretical Exploration on the Reason Why a Series of Similar Organic Molecules Exhibit Different Luminescence Types. *J. Phys. Chem. C* **2018**, *122*, 23091−23101.

(44) (a) Morris, S. A.; Wang, J.; Zheng, N. The Prowess of Photogenerated Amine Radical Cations in Cascade Reactions: From Carbocycles to Heterocycles. *Acc. Chem. Res.* **2016**, *49*, 1957−1968.

(45) Beatty, J. W.; Stephenson, C. R. J. Synthesis of (−)-Pseudotabersonine, (−)-Pseudovincadifformine, and (+)-Coronaridine Enabled by Photoredox Catalysis in Flow. *J. Am. Chem. Soc.* **2014**, *136*, 10270−10273.

(46) Choi, G. J.; Zhu, Q.; Miller, D. C.; Gu, C. J.; Knowles, R. R. Catalytic Alkylation of Remote C−H bonds Enabled by Proton-Coupled Electron Transfer. *Nature* **2016**, *539*, 268−271.

(47) Zhang, X.; Liu, L.; Li, W.; Wang, C.; Wang, J.; Fang, W.-H.; Chen, X. Extended Single-Electron Transfer Model and Dynamically Associated Energy Transfer Event in a Dual-Functional Catalyst System. *JACS Au* **2023**, *3*, 1452−1463.